

Impact of radiometric correction on the processing of UAV images

Piotr Kędziorski¹✉, Tomasz Kogut², Tomasz Oberski³

¹ <https://orcid.org/0000-0001-7753-2388>

² <https://orcid.org/0000-0001-9646-275X>

³ <https://orcid.org/0000-0002-0985-3363>

^{1,3}Koszalin University of Technology, Department of Geodesy and Geoinformatics
2 Śniadeckich St., 75-453 Koszalin, Poland

² Maritime University of Szczecin, Department of Geodesy and Offshore Survey
46 Żołnierska St., 71-250 Szczecin, Poland

e-mail: {¹piotr.kedziorski; ³tomasz.oberski}@tu.koszalin.pl, ²t.kogut@pm.szczecin.pl

✉ corresponding author

Keywords: remote sensing, drone, UAV, vegetation index, radiometric correction, Pix4D

JEL Classification: Y91, Q19, Q15

Abstract

Radiometric correction is a process that is often neglected when developing unmanned aerial vehicle (UAV) images. The aim of the work was to test the radiometric correction of images taken from a Parrot Sequoia+ camera mounted on UAV. Therefore, a script was written in Matlab environment to enable radiometric correction of the obtained images. The images were subjected to the correction process using the Matlab script and the commercial software Pix4D. The results were compared, and the study found a significant improvement in the radiometry in both cases. The computational process eliminated the influence of variable in-flight insolation caused by cloud cover. The software developed for the article was found to be as good as the commercial one.

Introduction

Recent progress in unmanned aerial vehicles (UAV) technologies and high-performance digital cameras allows multispectral photos to be obtained using a drone. This simple method gives access to high-resolution images at low expenses, contrary to satellite and aerial images, which do not provide sufficient resolution (Gago et al., 2015; Sankaran et al., 2015; Zaman-Allah et al., 2015; Yang et al., 2017). The photographic material delivered from UAVs enables the analysis of very small areas. The use of drones has an undoubtedly greater advantage over satellite imagery, including the possibility of adjusting the time of the surveys to meet specific needs (Launay & Guerif, 2005; Inoue et al., 2012).

The method is readily used in commercial, scientific, and military environments due to its versatility. Data obtained from the drone's ceiling can be used in remote sensing to determine vegetation indicators (Duan et al., 2014; Verger et al., 2014; Aasen et al., 2015; Sankaran et al., 2015; Jin et al., 2017; Zhou et al., 2017). However, in order to take full advantage of the potential of multispectral imaging, it is necessary to carry out radiometric correction (Deng et al., 2018). This procedure eliminates negative phenomena affecting the radiometry of the image and makes its analysis easier.

Radiometric correction is an initial process performed on digital images obtained by satellite, aerial, or short-range techniques. Depending on the data source, the calculation process may vary, but the

goal remains the same – to eliminate errors affecting the image radiometry and convert digital numbers (DN) into irradiance. The task of image acquisition sensors is to register the radiation reflected from the surface of objects. However, the recorded data are affected by certain noise; therefore, the DN representing a terrestrial object is not equal to the measurement of the irradiance of this object from a short distance (terrestrial observations). This is due to the sensor properties, such as the color processing algorithm, camera settings, or vignetting as well as sensor errors, atmosphere impact, and sun position. During the radiometric correction process, we strive to eliminate these factors (Osińska-Skotak, 2007; Tagle, 2017).

Camera sensor calibration is the first step performed during the correction. It consists of converting DN into irradiance along with the simultaneous elimination of noise occurring in data records. This is the reverse of the calculation performed by the sensor when recording an image. This process is executed with the use of calibration models of the sensors, determined under laboratory conditions (Schowengerdt, 2006; Tagle, 2017; Adler, 2018). Atmospheric correction depends on the flight altitude and the characteristics of the tested object. It determines the influence of the atmosphere and aerosols on the signal reaching the sensor. This signal is modified by the absorption and dispersion of gases. The elimination of atmospheric effects is the most difficult element of radiometric correction. In the case of drone studies, these effects are often overlooked due to the low flight altitude. However, when the amount of aerosol or haze is high, aerosol sensors (Zarco-Tejada et al., 2013) or a layered physical dispersion model (Huang et al., 2013) can be used (Schowengerdt, 2006; Osińska-Skotak, 2007). Solar correction aims to eliminate photons that have reached the sensor by a different route different than direct reflection from the object. There are six paths by which a photon can reach the sensor: three basic paths and three more complex paths related to multiple reflections. The first is the reflection of photons from the object that reach the sensor directly. The photons traveling this path represent the pixel value; the other paths are the noise, which we aim to eliminate. Two noise paths have the greatest impact: the scattering of light through the atmosphere toward the object and reflection from it to the sensor (sky shine), and the scattering of photons in the atmosphere, which reach the sensor without contacting the Earth's surface (upwelled radiance). The remaining paths are associated with multiple reflections

from the surface or the atmosphere; therefore, their energy is low, so they do not have a significant effect on the determination of the DN by the sensor (Schott, 2007).

A comprehensive study of the Parrot Sequoia+ camera along with a sun sensor was conducted by Olsson et al. (Olsson et al., 2021). In that study, they analyzed the effects of factors such as temperature and atmosphere on the radiometry of images. They used a calculation process proposed by the camera's manufacturer and compared the results with field measurements using a spectrometer. According to their study, reflections from the Parrot Sequoia+ camera were slightly lower than those from the field measurement. The correlation between the data and the camera and the field measurement was highest for the red band, followed by the near infrared, red-edge, and green bands. The high correlation of the red and near-infrared bands produced accurate normalized difference vegetation index (NDVI) values. The Parrot Sequoia+ camera and its radiometric accuracy were also studied by Teixeira et al. (Teixeira et al., 2020), who performed radiometric correction using Agisoft software. They used field measurements as reference data. They presented two cases: one with the correction performed solely on the basis of the light sensor and one that used a calibration target in addition to the light sensor. According to their research, correction should not be performed based solely on the light sensor, because the results are not satisfactory. Instead, the correction using the light sensor and calibration target performed in Agisoft software correlates very well with data from ground measurements. Delavarpour et al. also presented the problem of radiometric correction in their paper on the issue of UAV use in precision agriculture (Delavarpour et al., 2021). They cited 7 algorithms and two commercial software: Pix4D and Agisoft. However, they concluded that most of the correction method is too labor-intensive and does not give acceptable quality when used for precision agriculture.

In addition, there are cases in the literature regarding the study of the Parrot Sequoia+ camera in terms of its radiometry. However, most of the work focuses on comparing one method of radiometric correction to field measurements. In our work, we wanted to compare the application of two different correction methods. The aim of this study was to test the impact of radiometric correction of images from a Parrot Sequoia+ using two algorithms. The correction process recommended by the camera manufacturer was implemented in the Matlab environment

and compared with the algorithm provided by the commercial Pix4D software.

Methodology

There are many methods for carrying out radiometric corrections, ranging from the simplest one-point calibrations to the more complicated ones, such as calibration using a simplified empirical line or a method using a light sensor. The calculation recommended by the manufacturer of the Parrot Sequoia+ camera was chosen for the purpose of this study. The process consists of several steps presented in Figure 1. All steps should be repeated using images from each spectral range. The elements necessary for the computation process are found in the metadata of each image under the XMP label.

The first step is to eliminate the effect of vignetting on the pixel values of the image. Vignetting is the corner-darkening effect of a photo that appears as a function of the distance from the center of the image. To eliminate it, a 2D polynomial model provided by the camera manufacturer was used. In this model, for a given pixel p , its vignetting v affects the intensity of the incoming radiation depending on its position (x, y) as follows (Parrot for Developers, 2017a):

$$p(x_p, y_p) = v(x_p, y_p) \cdot i(x_p, y_p) \quad (1)$$

where: p – pixel value; v – vignetting function; i – irradiance for a given pixel.

Vignetting is a continuous function with respect to pixel coordinates, so it can be represented as a polynomial $v(x, y)$ and expressed by the following formula (Parrot for Developers, 2017a):

$$v(x, y) = \sum_{n,m} c_{n,m} x^n y^m \quad (2)$$

where: v – vignetting correction; n, m – a pair of powers of the x and y variables obtained from the metadata with the Xmp.Camera.VignettingPolynomial2DName label; $c_{n,m}$ – coefficient obtained from metadata labeled Xmp.Camera.VignettingPolynomial2D; x, y – pixel coordinates in the polynomial system.

After transforming the image coordinates into polynomial coordinates by dividing each pixel coordinate into the image size, the final formula for the vignetting correction was obtained (Parrot for Developers, 2017a):

$$v(x, y) = \sum_{n,m} c_{n,m} \left(\frac{x_p}{w} \right)^n \left(\frac{y_p}{h} \right)^m \quad (3)$$

where: x_p, y_p – pixel coordinates in the image system; w, h – width and height of the image in the pictorial layout.

The next step is to convert the DN to the irradiance using the following formula (Parrot for Developers, 2017b):

$$I = f^2 \frac{p - B}{A\epsilon\gamma + C} \quad (4)$$

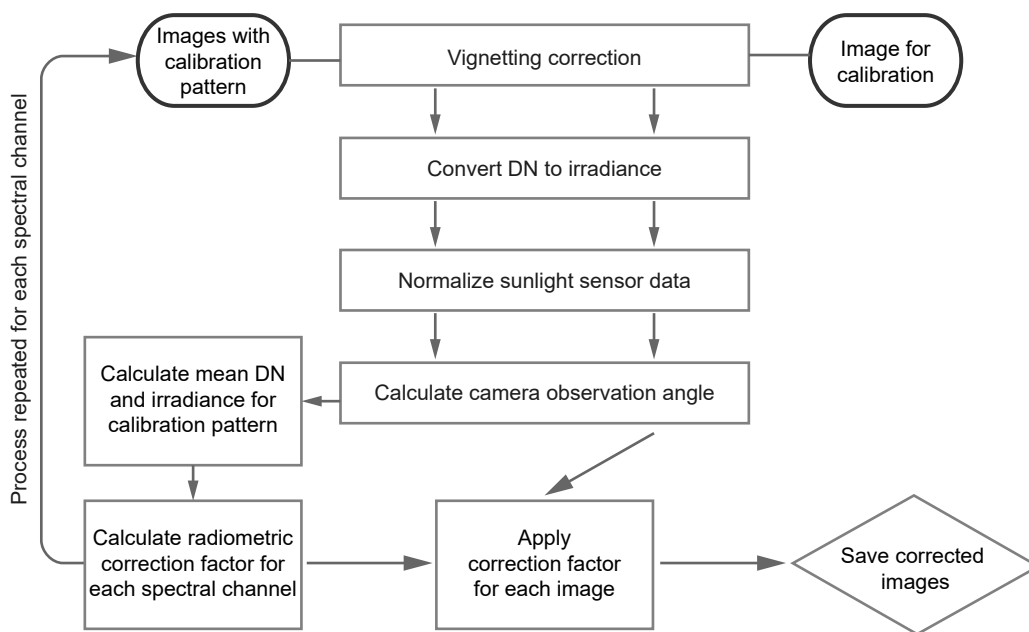


Figure 1. Diagram of the calculation process

where: p – pixel value; ε – exposure time in seconds; γ – ISO; f – focal length; I – irradiance; A, B, C – sensor calibration coefficients from Xmp.Camera.SensorModel metadata.

With the images converted into the irradiance, it is possible to go to the last correction step. The correction process is performed using the correction factor K based on the following formula (Parrot for Developers, 2017c):

$$R \cos \rho = K \frac{I_{sq}}{I_{ss}} \quad (5)$$

where: R – corrected value of reflectance; ρ – observation angle; I_{sq} – irradiance captured by the Parrot Sequoia+; I_{ss} – irradiance captured by sunshine sensor; K – calibration coefficient.

By analyzing formula (5), it can be seen that the calculation requires the camera observation angle and the sunlight sensor readings. Calculations based on formula (6) are enough to establish the camera tilt angle. The data on the sunlight sensor are stored in the metadata, but they are encoded in BASE64. So, the first step is to decode them. The sensor can take readings in four standards; for each of them, CH0 and CH1 coefficients have been defined. To calculate the sunlight sensor irradiance using formula (7), first the readings should be normalized to one selected standard using formula (8) (Parrot for Developers, 2017c).

$$\cos \rho = \frac{\cos \theta \cos \phi}{\sqrt{(-\sin \theta)^2 + (\cos \theta \sin \phi)^2 + (\cos \theta \cos \phi)^2}} \quad (6)$$

where: ρ – yaw, ϕ – roll, θ – pitch.

$$v_z = v_s / \frac{g_p}{g_w} \quad (7)$$

where: v_z – CH0 value normalized to the selected standard; g_p – CH0 gain factor for the standard in which the measurement was performed; g_w – CH0 gain factor for the standard we want to switch to; v_s – CH0 value obtained by the sensor.

$$I_{ss} = \frac{v_z}{g \tau} \quad (8)$$

where: I_{ss} – irradiation read by the sunshine sensor; v_z – normalized CH0 value; g – relative gain factor; τ – exposure time of sunshine sensor.

All the above data are used in the calculation of the radiometric correction factor using the following formula (Parrot for Developers, 2017c):

$$K = R \frac{I_{ss}}{I_{sq}} \cos \rho \quad (9)$$

The calibration factor must be calculated separately for each spectral channel and then applied to each image in a given spectral range according to formula (5). Photos with improved radiometry were obtained this way.

Research area data acquisition and processing

The object of research was the church of St. Mother Teresa of Calcutta, located in the northern part of the city of Koszalin in the Jamno district. The entire surroundings of the 14th-century church with numerous trees and grassy vegetation were measured. Figure 2 shows the approximate area of the study.



Figure 2. Research area (Geoportal, 2022)

The data used in the study were obtained with a Parrot Sequoia+ camera. The camera enables shooting in four spectral ranges (green, red, red-edge, infrared) and the visible RGB range. It was assembled on the DJI Phantom 4 Advanced drone. Additionally, the system was equipped with a sun sensor constructed of four sensors, one for each spectral range. Table 1 shows the exact specification of the camera and sunshine sensor.

Table 1. Specifications of the Parrot Sequoia+ and the sunshine sensor

Main Unit	Dimensions	59 mm × 41 mm × 28 mm
	Weight	72 g
RGB Camera	Camera Resolution	16 MP
	Image size	4608 × 3456 pixels
	Shutter release	Rolling shutter
	Focal length	4.88 mm
Multispectral Camera	Camera Resolution	1.2 MP
	Image size	1280 × 960 pixels
	Shutter release	Global shutter
	Focal length	3.98 mm
	Wavelengths	Green 550 nm (40 nm width) Red 660 nm (40 nm width) Red-edge 735 nm (10 nm width) Near infrared 790 nm (40 nm width)
	Additional features	Internal motion unit (IMU), magnetometer
Sunshine Sensor	Dimensions	47 mm × 39.6 mm × 18.5 mm
	Weight	35 g
	Spectral sensors	Green, red, red-edge, near infrared
	Additional features	Global positioning system (GPS), IMU, magnetometer

The fieldwork took place on October 19, 2019. The drone was sent on a previously planned route guided in autopilot mode. Shutter release at a specified time was programmed. Some 665 files were collected during the flight, which gave 133 camera positions. However, 88 positions were selected for the study, because the camera took pictures throughout the flight, and thus also during the take-off and landing of the UAV. Before the flight, the correction panel was photographed.

In order to carry out the radiometric correction by means of the previously presented calculation process, software in the Matlab environment was implemented. With the use of this script, radiometric

correction of all acquired photos was made. Then, using Pix4D software, three sets of orthomosaics were created. Each set contained four mosaics representing the spectral ranges (red, green, red-edge, near infrared) and one mosaic of the NDVI vegetation index. The first set of mosaics was created based on photos with no correction process applied. The second set was based on photos subjected to the computational process presented in this study. In the third set, photos after correction by the Pix4D program were used.

Results and discussion

The comparison of the NDVI index determined using the above data is the most important element of the analysis because the radiometric correction was performed to improve the quality of the indicators.

Figure 3 shows the index determined from the photos without correction. Infrastructure elements such as buildings and pavements take values from about -0.4 to 0.1 , whereas vegetation varies from 0 to 0.8 . In the north-western part, near the church in the center of the study, there are places where the index is around 0.2 for vegetation. When analyzing the histogram, four characteristic peaks can be seen. The first one is on the value -0.325 , which refers to the upper left corner of the study and shows a clear decrease in the value of the factor. Two consecutive peaks at -0.1 and 0.1 represent the infrastructure. The last, widest peak located around 0.55 has values corresponding to the photographed vegetation.

Figure 4 shows the index with mosaic No. 2 using the Matlab script. The first element that stands out is the reduction of the NDVI value for non-vegetal areas. At the same time, the index increases for flora, which has clarified the contrast between these elements. The spots with small values mentioned in the description of Figure 3 have been significantly leveled, but slight discoloration is still visible. The histogram of this study is changed compared to the original one. The min and max values were increased by which the histogram stretched. The shape has also changed. Now two separate peaks occur: one at -0.15 , the other at 0.7 . A transition is created at a height of 0.2 : the values on the left are the number of pixels representing buildings etc., and on the right are green areas.

The last orthomosaic in Figure 5 was made after correction in Pix4D. Compared to the previous two, a significant increase in the value of green objects can be observed. Most of the vegetation has an index of 0.5 to 0.9 . There is also an increase in the building

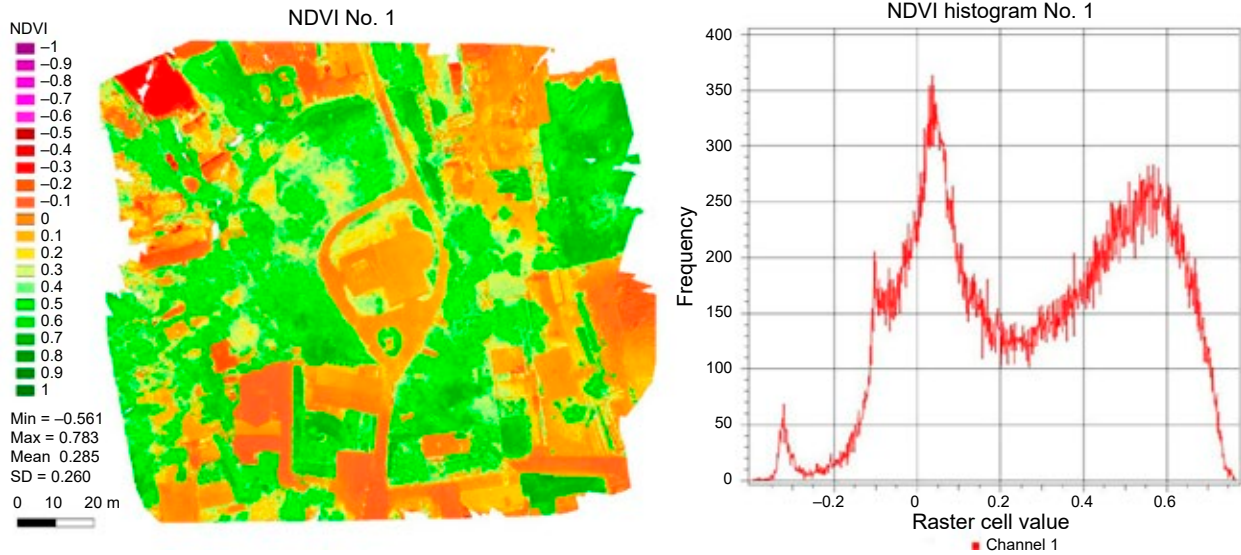


Figure 3. NDVI index No. 1

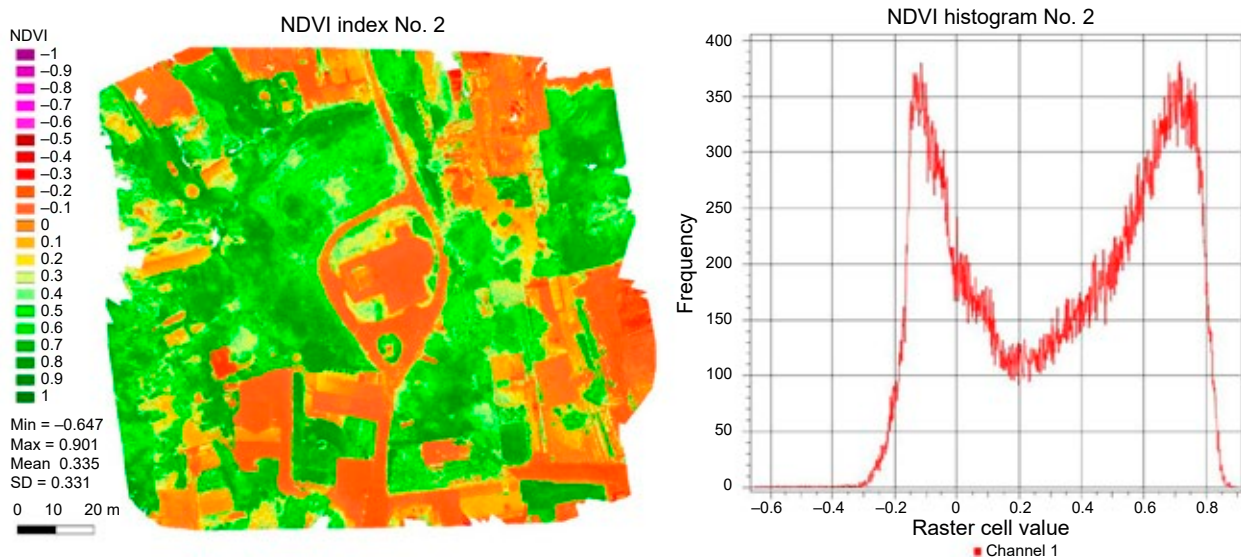


Figure 4. NDVI index No. 2

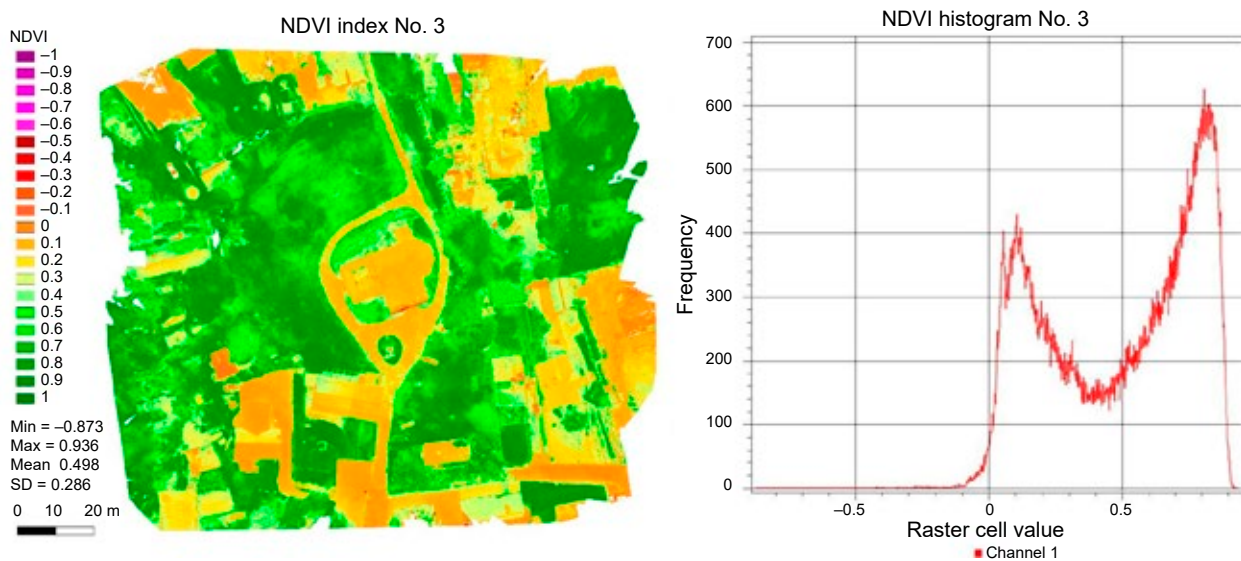


Figure 5. NDVI index No. 3

coefficient of around 0.1. Vegetation changes in the northwest have been almost eliminated. In the histogram, it is clear that the range has been shifted to the right. Almost the entire diagram is on the positive side of the axis. In this case, there are also two peaks, but the first is around 0.1, and the second is around 0.9.

By comparing all three studies, it can be concluded that both radiometric correction algorithms work successfully. The algorithm used in the proprietary program increases the amplitude to a value of about 0.85 by reducing the ratio for infrastructure and increasing it for vegetation, which improves the contrast. However, some vegetation still has a relatively low index, which would indicate its poor condition. One might conclude that values below 0 represent non-plant elements. Values in the range 0 to 0.2 describe the unnatural parts as well as the less conditioned vegetation. However, values above 0.2 refer only to vegetation. This is similar to Pix4D. An amplitude of 0.9 gives a comparable contrast, while the entire range of values is shifted to the positive part of the axis. High contrast creates a clear transition between the vegetation and other elements. In this case, values below 0.3 refer to infrastructure and those above 0.3 to vegetation.

The next step is the analysis of the difference rasters, showing how the values of the NDVI coefficient have changed on individual mosaics.

The first case shown in Figure 6 is the difference between mosaics No. 1 and 2. This was obtained by subtracting from mosaic No. 2 the value of mosaic No. 1, so it represents the correction value that was introduced. When analyzing the picture,

a characteristic spot in the upper left corner with a difference of about 0.25 is visible. In the opposite lower right corner, there is a difference of -0.15 to -0.20 . The differences in the infrastructure elements are around -0.20 to 0 and in the vegetation from 0 to 0.20 . Such a distribution would explain the contrast mentioned during the analysis of Figure 4. In the histogram, the differences between the two mosaics are at the level of -0.25 to 0.25 .

Figure 7 shows the difference raster between orthomosaics No. 1 and 3. This was obtained by subtracting mosaic No. 1 from mosaic No. 3. As in the previous picture, two areas can be seen in the extreme parts of the study area. The upper left corner ranges from 0.25 to 0.5 , and the right corner ranges from 0.05 to 0.20 . The rest of the study has a difference of 0 – 0.15 for buildings from 0.15 to 0.25 for vegetation. The histogram shows that for the entire study area, the differences in values are positive, so study No. 3 has values greater than study No. 1 in the entire area.

The last raster shown in Figure 8 was obtained by subtracting mosaic No. 2 from mosaic No. 3. This raster has no significant differences in any of the corners of the study area. The differences are relatively constant and amount to about 0.10 to 0.20 for vegetation and 0.20 to 0.30 for other elements. This shows that both algorithms, the one used in Matlab and the one used in Pix4D, are equally good.

When analyzing the images, it is not possible to ignore the characteristic spots on both differential rasters with the base raster as one of the elements. This may be caused by varying sunlight. By following the drone's flight path, some correlations can

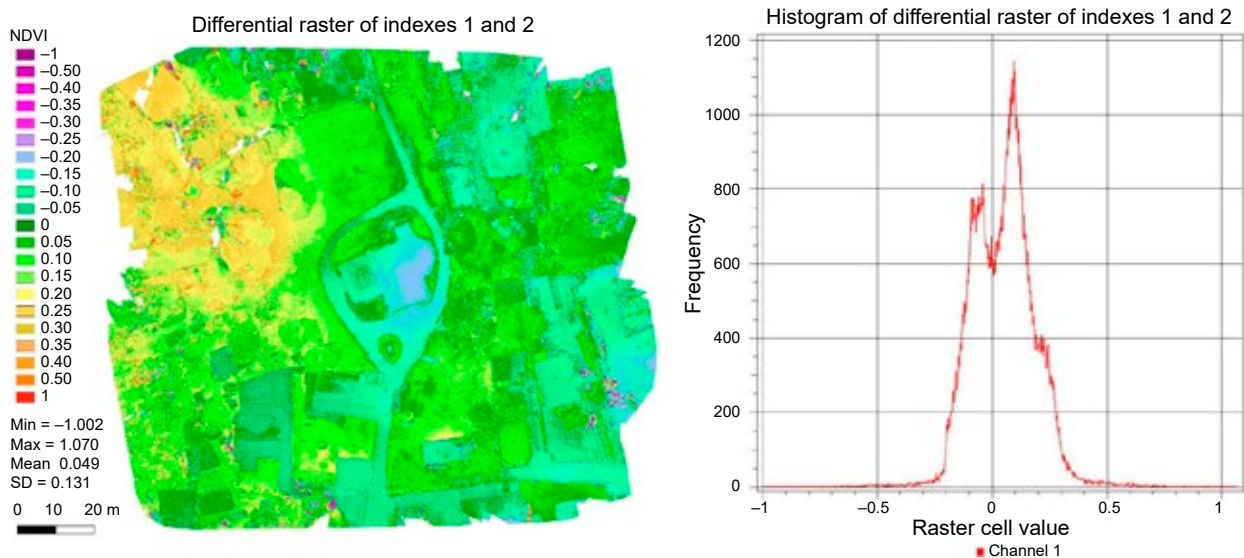


Figure 6. Differential raster of indexes 1 and 2

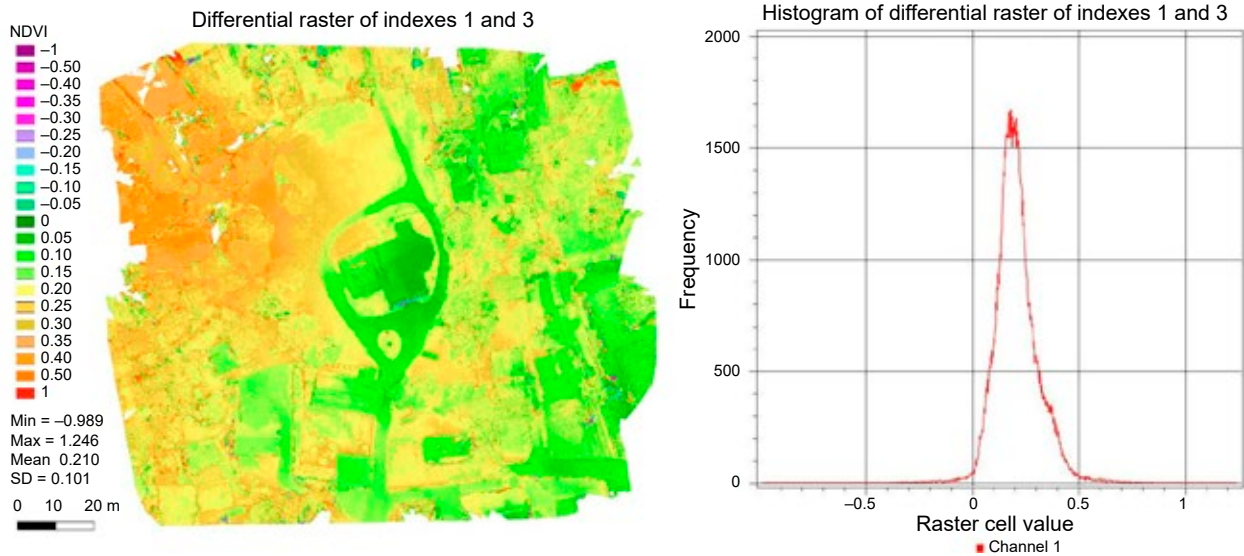


Figure 7. Differential raster of indexes 1 and 3



Figure 8. Differential raster of indexes 2 and 3

be found. The spots can be caused by a change in exposure during the flyby (e.g., the sun was behind the clouds at the beginning of the flyby and came out of them during the flight, causing a change in the top left). However, it should be noted that neither the orthomosaic in Figure 4 nor that in Figure 5 show clear changes in these areas. Therefore, both algorithms successfully eliminated the impact of changing insolation caused by clouds obscuring the sun during flight. The above analysis also confirms the differences between the buildings. One model subtracted the NDVI values from the buildings and the other either kept them unchanged or added small amounts. This resulted in a disproportion between the buildings of the order of 0.20 to 0.30. Figure 8

shows that the differences between the two methods of radiometric correction are constant. Both algorithms eliminated the effect of uneven sun exposure, and the final results are shifted relative to each other on the histogram axis only by about 0.1 for vegetation and 0.25 for infrastructure.

Conclusions

The results of the analyses show that both algorithms eliminated the negative impact of changing the intensity of sunlight during the drone's flight. Some differences were observed between the methodology recommended by the camera manufacturer and the commercial software. Both correction

processes were successful, and the obtained results were presented with some shift in the histogram axis. The shape of the histograms was preserved when the results were shifted relative to each other. In both cases, there was an improvement in the radiometry of the images, but the algorithm performed in Matlab resulted in a decrease in the NDVI value for anthropological objects, whereas the Pix4D algorithm kept this value at a comparable level and was in some regions slightly lower than the index obtained without any correction. Such results raise the question of which algorithm behaves better not only for vegetation but also for anthropogenic objects. This leaves room for further research and comparison of the two algorithms not only against each other but also against field measurements made with a spectrometer. Additional correction algorithms available in the literature could be included in such analyses. Furthermore, there is the possibility of creating a measurement field in which the behavior of the algorithms under different atmospheric and lighting conditions would be examined. Perhaps some algorithms could behave better on very sunny days and others under cloudy skies and high aerosol content in the atmosphere. Such a study could show the current state of knowledge on correction techniques and the possible need for new algorithms.

References

1. AASEN, H., BURKART, A., BOLTEN, A. & BARETH, G. (2015) Generating 3D hyperspectral information with lightweight UAV snapshot cameras for vegetation monitoring: From camera calibration to quality assurance. *ISPRS Journal of Photogrammetry and Remote Sensing* 108, pp. 245–259.
2. ADLER, K. (2018) *Radiometric correction of multispectral images collected by a UAV for phenology studies*. Thesis for Master of Science. Uppsala, Sweden: Swedish University of Agricultural Sciences.
3. DELAVARPOUR, N., KOPARAN, C., NOWATZKI, J., BAJWA, S. & SUN X. (2021) A Technical Study on UAV Characteristics for Precision Agriculture Applications and Associated Practical Challenges. *Remote Sensing* 13(6), 1204.
4. DENG, L., YAN, Y., GONG, H., DUAN, F. & ZHONG, R. (2018) The effect of spatial resolution on radiometric and geometric performances of a UAV-mounted hyperspectral 2D imager. *ISPRS Journal of Photogrammetry and Remote Sensing* 144, pp. 298–314.
5. DUAN, S.-B., LI, Z.-L., WU, H., TANG, B.-H., MA, L., ZHAO, E. & LI, C. (2014) Inversion of the PROSAIL model to estimate leaf area index of maize, potato, and sunflower fields from unmanned aerial vehicle hyperspectral data. *International Journal of Applied Earth Observation and Geoinformation* 26, pp. 12–20.
6. GAGO, J., DOUTHE, C., COOPMAN, R.E., GALLEGO, P.P., RIBAS-CARBO, M., FLEXAS, J., ESCALONA, J. & MEDRANO, H. (2015) UAVs challenge to assess water stress for sustainable agriculture. *Agricultural Water Management* 153, pp. 9–19.
7. Geoportal (2022) <https://mapy.geoportal.gov.pl> [Accessed: March 09, 2022].
8. HUANG, Y., THOMSON, S., HOFFMANN, C., LAN, Y. & FRITZ, B. (2013) Development and prospect of unmanned aerial vehicle technologies for agricultural production management. *International Journal of Agricultural and Biological Engineering* 6(3), pp. 1–10.
9. INOUE, Y., SAKAIYA, E., ZHU, Y. & TAKAHASHI, W. (2012) Diagnostic mapping of canopy nitrogen content in rice based on hyperspectral measurements. *Remote Sensing of Environment* 126, pp. 210–221.
10. JIN, X., LIU, S., BARET, F., HEMERLÉ, M. & COMAR, A. (2017) Estimates of plant density of wheat crops at emergence from very low altitude UAV imagery. *Remote Sensing of Environment* 198, pp. 105–114.
11. LAUNAY, M. & GUERIF, M. (2005) Assimilating remote sensing data into a crop model to improve predictive performance for spatial applications. *Agriculture, Ecosystems & Environment* 111, pp. 321–339.
12. OLSSON, P.-O., VIVEKAR, A., ADLER, K., GARCIA MILLAN, V. E., KOC, A., ALAMRANI, M. & EKLUNDH, L. (2021) Radiometric Correction of Multispectral UAS Images: Evaluating the Accuracy of the Parrot Sequoia Camera and Sunshine Sensor. *Remote Sensing* 13(4), 577.
13. OSIŃSKA-SKOTAK, K. (2007) The importance of radiometric correction in satellite images processing (in Polish). *Archiwum Fotogrametrii, Kartografii i Teledetekcji* 17b, pp. 577–590.
14. Parrot for Developers (2017a) SEQ AN 02 – How to correct vignetting in images. [Online]. Available from: https://forum.developer.parrot.com/t/parrot-announcement-release-of-application-notes/5455?source_topic_id=6558 [Accessed: March 09, 2022].
15. Parrot for Developers (2017b) SEQ AN 01 – Pixel to Irradiance. [Online]. Available from: https://forum.developer.parrot.com/t/parrot-announcement-release-of-application-notes/5455?source_topic_id=6558 [Accessed: March 09, 2022].
16. Parrot for Developers (2017c) SEQ AN 04 – How to correct distortion in images. [Online]. Available from: https://forum.developer.parrot.com/t/parrot-announcement-release-of-application-notes/5455?source_topic_id=6558 [Accessed: March 09, 2022].
17. SANKARAN, S., KHOT, L.R., ESPINOZA, C.Z., JAROLMASJED, S., SATHUVALLI, V.R., VANDEMARK, G.J., MIKLAS, P.N., CARTER, A.H., PUMPHREY, M.O., KNOWLES, N.R. & PAVEK, M.J. (2015) Low-altitude, high-resolution aerial imaging systems for row and field crop phenotyping: A review. *European Journal of Agronomy* 70, pp. 112–123.
18. SCHOTT, J.R. (2007) *Remote Sensing: The Image Chain Approach*. Oxford University Press, USA.
19. SCHOWENGERDT, R.A. (2006) *Remote Sensing: Models and Methods for Image Processing*. Elsevier Science.
20. TAGLE, X. (2017) *Study of radiometric variations in Unmanned Aerial Vehicle remote sensing imagery for vegetation mapping*. Thesis for Master of Science. Iquitos, Loreto, Peru: Instituto de Investigaciones de la Amazonía Peruana. Available from: <https://doi.org/10.13140/RG.2.2.16940.36485>.
21. TEIXEIRA, A.A.D., MENDES, C.W. JÚNIOR, BREDEMEIER, C., NEGREIROS, M. & AQUINO, R. (2020) Evaluation of the radiometric accuracy of images obtained by a sequoia multispectral camera. *Engenharia Agrícola* 40, 6, pp. 759–768.

22. VERGER, A., VIGNEAU, N., CHÉRON, C., GILLIOT, J.-M., COMAR, A. & BARET, F. (2014) Green area index from an unmanned aerial system over wheat and rapeseed crops. *Remote Sensing of Environment* 152, pp. 654–664.
23. YANG, G., LIU, J., ZHAO, C., LI, ZHENHONG, HUANG, Y., YU, H., XU, B., YANG, X., ZHU, D., ZHANG, X., ZHANG, R., FENG, H., ZHAO, X., LI, ZHENHAI, LI, H. & YANG, H. (2017) Unmanned Aerial Vehicle Remote Sensing for Field-Based Crop Phenotyping: Current Status and Perspectives. *Frontiers in Plant Science* 8, doi: 10.3389/fpls.2017.01111.
24. ZAMAN-ALLAH, M., VERGARA, O., ARAUS, J.L., TAREKEGNE, A., MAGOROKOSHO, C., ZARCO-TEJADA, P.J., HORNERO, A., ALBÀ, A.H., DAS, B., CRAUFURD, P., OLSEN, M., PRASANNA, B.M. & CAIRNS, J. (2015) Unmanned aerial platform-based multi-spectral imaging for field phenotyping of maize. *Plant Methods* 11, 35.
25. ZARCO-TEJADA, P., MORALES, A., TESTI, L. & VILLALOBOS, F. (2013) Spatio-temporal patterns of chlorophyll fluorescence and physiological and structural indices acquired from hyperspectral imagery as compared with carbon fluxes measured with eddy covariance. *Remote Sensing of Environment* 133, pp. 102–115.
26. ZHOU, X., ZHENG, H.B., XU, X.Q., HE, J.Y., GE, X.K., YAO, X., CHENG, T., ZHU, Y., CAO, W.X. & TIAN, Y.C. (2017) Predicting grain yield in rice using multi-temporal vegetation indices from UAV-based multispectral and digital imagery. *ISPRS Journal of Photogrammetry and Remote Sensing* 130, pp. 246–255.

Cite as: Kędziorski, P., Kogut, T., Oberski, T. (2023) Impact of radiometric correction on the processing of UAV images. *Scientific Journals of the Maritime University of Szczecin, Zeszyty Naukowe Akademii Morskiej w Szczecinie* 73 (145), 5–14.